Journal of
Manufacturing and Materials Processing

MDPI

Article

Weldability Assessment of Austenitic/Ferritic Clad Plates Joined by a Combined Laser Beam–Electric Arc Process

Girolamo Costanza [1], Fabio Giudice [2,*], Severino Missori [1], Cristina Scolaro [3], Andrea Sili [3,*] and Maria Elisa Tata [1]

[1] Department of Industrial Engineering, University of Rome-Tor Vergata, 00133 Roma, Italy; costanza@ing.uniroma2.it (G.C.); missori@uniroma2.it (S.M.); elisa.tata@uniroma2.it (M.E.T.)
[2] Department of Civil Engineering and Architecture, University of Catania, 95123 Catania, Italy
[3] Department of Engineering, University of Messina, 98166 Messina, Italy; cscolaro@unime.it
* Correspondence: fabio.giudice@unict.it (F.G.); asili@unime.it (A.S.)

Abstract: The combined use of laser beam and electric arc for welding thick clad steel plates in a single pass has been developed to solve the issues concerning the individual applications of the heat sources, such as the low filling efficiency of conventional electric arc methods and the drawbacks concerning laser beam defects due to rapid cooling and solidification. This work was addressed to the weldability assessment of ferritic steel plates, clad with austenitic stainless steel, under the laser-leading configuration, testing the effects of two different values of the inter-distance between the laser beam and the electric arc. Specimens of the welded zone were investigated by metallographic observations and EDS measurements; mechanical properties were characterized by the Vickers microhardness test and by the FIMEC instrumented indentation test to obtain the local values of the yield strength. Welding simulations by theoretical modelling were also carried out to outline the differences in the thermal fields generated by the two heat sources, their interaction, and their effect on the configurations of the weld pool and the thermal profiles to which the materials are subjected. The welding setup with higher inter-distance was more suitable for joining clad steel plates, since the action of the deep keyhole mode is substantially separated from that of the shallower electric arc. In this way, the addition of alloying elements, performed by melting the filler wire, concentrated in the cladding layer, helping maintain the austenitic microstructure, while the laser beam acts in depth along the thickness, autogenously welding the base steel.

Keywords: combined welding; weldability; clad steel; fused zone; heat affected zone

check for updates

Academic Editor: Antonio Riveiro

Received: 31 January 2025
Revised: 2 March 2025
Accepted: 6 March 2025
Published: 11 March 2025

Citation: Costanza, G.; Giudice, F.; Missori, S.; Scolaro, C.; Sili, A.; Tata, M.E. Weldability Assessment of Austenitic/Ferritic Clad Plates Joined by a Combined Laser Beam–Electric Arc Process. *J. Manuf. Mater. Process.* **2025**, *9*, 90. https://doi.org/10.3390/jmmp9030090

Copyright: © 2025 by the authors. Licensee MDPI, Basel, Switzerland. This article is an open access article distributed under the terms and conditions of the Creative Commons Attribution (CC BY) license (https://creativecommons.org/licenses/by/4.0/).

1. Introduction

Conventional methods for welding thick steel plates are based on many passes where the heat input is generated by an electric arc and the filler metal is introduced in the form of a continuous wire [1]. In this form, welding is a laborious process that accounts for a considerable part of the working time and cost. Thick plates require large grooves with beveled edges, which can be filled with a slowly travelling electric arc resulting in high heat input and residual stress [2].

Laser-Arc Hybrid Welding (LAHW) is considered a valid solution for joining thick plates thanks to the high energy density and deep penetration. It requires an expensive set up but offers the benefit of fast welding speed and focused high-power density [3].

In the keyhole mode, typical of high-power Laser Beam Welding (LBW), the weld area is minimized, resulting in narrow high-quality welds. However, LBW tends to pro-

duce a hard martensitic microstructure due to high cooling rates [4]; furthermore, this technique can lead to issues such as high-temperature cracking, underfill, and internal pore formation or defects due to rapid cooling and solidification [5]. These shortcomings can be overcome by using hybrid welding technology consisting of a laser beam coupled with an electric arc, a method developed at the end of the 1970s and presently highly valued in the petrochemical and automotive industries, as well as in shipbuilding.

LAHW combines, in a synergic way, the advantages of the laser beam, with its high power density, and the electric arc, typically characterized by good bridgeability of the joint gap due to the introduction of the filler metal.

The simultaneous action of these heat sources influences the formation of the weld pool, allowing the welding of thick plates in a single pass. In Figure 1, the typical cross-sections obtained by multi-pass arc welding, LBW, and LAHW are compared [6]. The shape of the LAHW joints resemble a wine glass and can be divided into two parts, as in Figure 1c where the red line separates the wide zone principally affected by the electric arc heat input from the narrow one due to the keyhole welding mode [7]. Recently, Gook et al. [8] highlighted the presence of an upper arc zone characterized by the alloying effect of the filler wire; however, this action decreases along the keyhole towards the weld root.

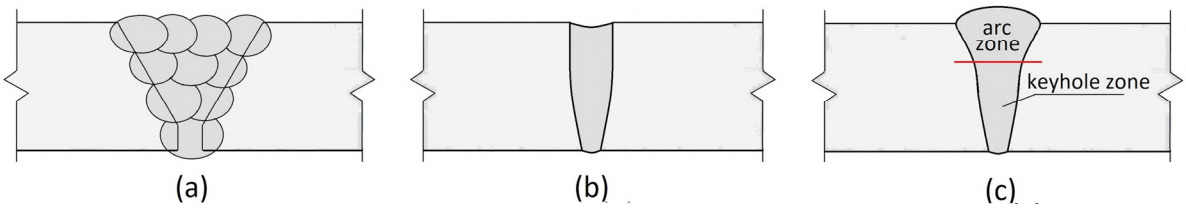


Figure 1. Sketches of the sections obtained respectively by: (**a**) Multi-pass arc welding; (**b**) Single pass of LBW; (**c**) Single pass of LAHW.

Re-heating and re-melting problems, which affect the multi-pass process of arc welding, can be overcome by working in a single pass. Therefore, LAHW results in high filling efficiency, allowing us to obtain weldments with better properties than with the traditional welding methods [9]. Recently, Zhang et al. [10] LAHWed, with only three passes, two butt-positioned plates of Q355B steel, 20 mm thick; Brunner-Schwer et al. [11] showed, by joining the 25 mm thick steel structures of a wind tower in a single pass, the ability of the LAHW process to reduce working time and increase productivity when compared to Submerged Arc Welding (SAW). In particular, the LAHW process time is reduced by more than 80%, and the process cost is reduced by up to 90%. Recently, Bunaziv et al. [12] demonstrated, through a comparative study, that LAHW consumes significantly less energy and requires less working time than Gas Metal Arc Welding (GMAW); in addition, due to less beveling of the plates, the filler usage in LAHW is significantly lower than in GMAW. In other words, LAHW is more efficient than the well-established arc welding method in terms of sustainability.

Compared with LBW, LAHW represents a better solution because the heat input of the arc provides a moderate cooling rate, which can lead to reduced hardness; furthermore, by adding a filler wire with suitable composition, more favorable microstructures can be obtained. Since the presence of the electric arc leads to a higher tolerance to any misalignments, LAHW also shows better bridgeability than LBW. However, strict control of the heat input is required to avoid the onset of residual stress and distortions, which could be slightly higher than in LBW [4].

Figure 2 shows the two possible configurations of the hybrid process: laser-leading or arc-leading. The choice of one of these two variants leads to different features of the weld

geometry, penetration depth, and the microstructures of the fusion zone (FZ) and the heat affected zone (HAZ).

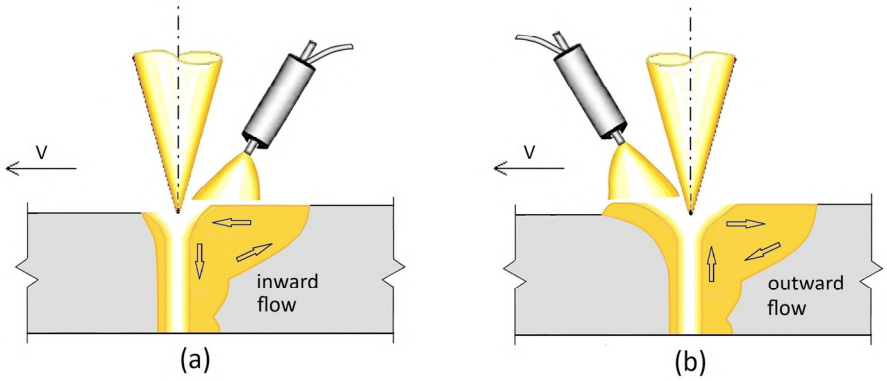


Figure 2. LAHW configurations (vector v represents the welding speed direction): (**a**) Laser beam leading; (**b**) Arc leading.

In [13], the authors experimented with these two configurations for butt-welding two mild steel plates (10 mm thick) in a single pass. When the laser beam precedes the arc (Figure 2a), the molten metal flow is inward; consequently, the alloying elements of the filler wire can be distributed towards the keyhole bottom in a more efficient way than in the arc-leading configuration.

Conversely, in the arc-leading configuration (Figure 2b), the metal flow is outward, causing a less homogeneous distribution of the filler. In any case, this arrangement gives a more stable arc and deeper penetration. The latter is presumably due to the fact that the laser beam impinges the melt pool with better absorption than a solid surface, reducing the energy loss from the laser through heat conduction [14]. Furthermore, in [2], the authors proved that the arc-leading configuration helps to prevent the formation of a hump at the weld root and has higher electrical stability than the laser-leading configuration.

Due to the high welding speed used in LAHW, the wire feed rate should be set at a higher value. It requires a higher current rating to maintain the arc length at equilibrium; consequently, to prevent any damage, the torch is water-cooled. The dynamic interactions of the laser irradiation and the heat input of the electric arc, together with the filler metal droplet conditions, govern the shape of the weld bead [15]. The shape and the microstructural characteristics of weld depend on the ratio of laser power/electric power, which determines the balance between the effects of the two heat sources. In the qualitative form, it can be stated that when this ratio decreases, the process changes from being like laser welding to more closely resembling arc welding [7].

Steel plates of thicknesses up to 25 mm can be successfully welded using a hybrid 20 kW laser and Metal Active Gas (MAG) system in a single pass with a welding speed of 1 m/min [3]. Moreover, several authors demonstrated that the advantages of LAHW steel plates are not limited to the geometrical features and reduced presence of welding defects, but are also due to better metallurgical characteristics, as highlighted in [16] for high nitrogen austenitic steels. In particular, Yang et al. [17] showed how a proper choice of the arc current and the laser power leads to reduced porosity and hence to better mechanical strength in LAHW dissimilar medium/low carbon steels. In [6], the authors LAHWed low carbon steel plates, achieving satisfying quality joints with high mechanical strength and plasticity. Silva et al. [18] compared the microstructure of hardenable steels joined by LBW and LAHW, demonstrating the metallurgical and operational advantages of the hybrid process.

The inter-distance (d) between the laser plume and the arc impingement point is considered a crucial parameter: when it is too short, keyhole collapse may occur; therefore,

a certain distance between the laser and arc is desirable [5]. In any case, the value of this parameter needs to be adapted for each weld case according to the materials and several other parameters, such as joint type, welding configuration and speed, arc power and mode, and shielding gas. In [19], the authors used the arc leading configuration to weld 7 mm thick steel plates, showing that the synergy between laser and electric arc occurred for inter-distances not exceeding 5 mm. Usually, values in the range 2–3 mm were considered in literature [2,6,9,13].

In this regard, Kang et al. [20] observed that the process of welding austenitic steel plates becomes unstable when the laser-arc distance was either smaller than 1 mm or larger than 9 mm. Gao et al. [21] demonstrate, for 7 mm thick steel plates, that when this distance is less than 4 mm, the interaction between the laser induced plasma and the arc plasma is dominant; whereas, as this distance increases, a preheating action of the electric arc becomes prevalent. If the effect of the laser beam prevails, the melt pool could be too narrow, making it difficult for bubbles to escape and causing defects such as pores and cracks. Greater values of d lead towards a configuration where the electric arc does not directly affect the keyhole (tandem mode): in the case of leading laser beam, the trailing arc produces a short-time post-heating treatment of the weld that can improve the microstructure [14]. As a matter of fact, at higher laser-arc inter-distance, the heat sources become more separated, turning from a hybrid process with shared melt pools into a tandem process with an indirect interaction between the sources [22].

Gao et al. [23] experimented the tandem configuration with a trailing arc, maintaining a distance d = 40 mm between the two heat sources. This value implies the formation of a shallow melt pool due to the electric arc being separated from the keyhole, which acts in depth along the thickness. The trailing arc heats the weld produced by the laser beam, acting as secondary heat treatment and resulting in a reduction in the cooling rate and residual welding stress.

Figure 3 shows a sketch of the tandem welding mode in the laser leading configuration: the trailing torch is spaced so far away from the laser beam that the melt pool does not interfere with the keyhole. In this way, the weld bead will have two distinct zones: the upper one is affected by the action of the electric arc (here the transfer of the alloy elements occurs due to the melting of the welding wire), while the lower one is produced by the action of the keyhole and can be affected by the pre-post heating effect generated by the electric arc.

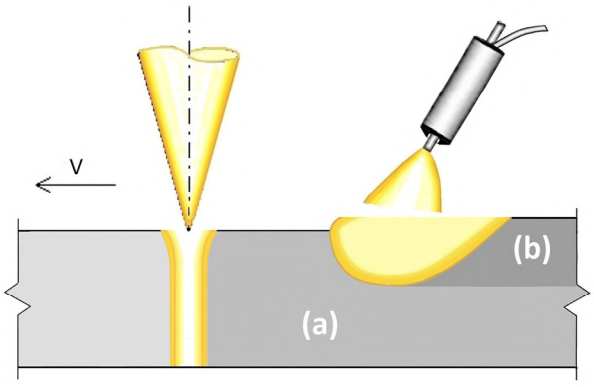


Figure 3. Sketch of the tandem configuration with indication of the welding speed v direction: (**a**) Deep weldment produced by the keyhole; (**b**) Shallow weldment due to the electric arc.

For its multiple advantages, the combined welding process is also carried out to join clad steel plates. The plates consist of a substrate of inexpensive carbon steel coated with a layer, usually of stainless steel or other more expensive metals, with high corrosion resistance, such as Ti, which confers specific metallurgical characteristics [24,25]. The

current technology allows a secure interface between the two metals, providing a viable and cost-effective alternative to the use of expensive alloys [26].

The traditional joining method consists of multiple passes of arc welding; consequently, the heating cycles affect the composition and metallurgical characteristics of both FZ and HAZ [27,28]. To overcome these shortcomings, different solutions have been proposed for welding clad steel plates in a single pass, such as LBW with filler metal interposed as consumable inserts between butt-positioned clad steel plates [29]. More commonly, the combined laser–arc process, with filler metal added by melting the electrode wire, is used; in general, to achieve a suitable composition of the FZ, this technique requires a careful choice of the experimental setup, as well as an accurate setting of the process parameters, as documented by several authors during the last two decades [10,30,31].

However, the case of clad steels is particularly laborious, as it is necessary to develop specific operating methods. Therefore, due to the complexity of the phenomena, the evaluation of the clad steel weldability must be equally accurate and targeted to the specific case.

With these premises, and considering that only a few articles in the literature have dealt with this topic, the purpose of the present work lies in the application of the laser-arc welding technique to join structural steel plates clad with an austenitic layer, carrying out a careful assessment of weldability by combining and correlating the experimental results of microstructural and local mechanical characterizations of the welded joint, as well as thermal field simulations.

Given the issues that emerge due to the simultaneous presence of ferritic and austenitic layers, a combined laser-arc process in a single pass was used to differentiate the composition of the weld at the two different levels of the cladding layer and the base metal. In addition to having successfully carried out the welding of thick clad plates in a single pass, the novelty of the present work consists in an accurate verification of weldability through experimental investigations and analytical evaluation of the thermal field. In this regard, a procedure for simulating the thermal fields in the case of clad steel was specifically developed by adapting a conduction-based theoretical model to the morphology of the weld cross-section detected experimentally.

The welding trials were carried out with the laser-leading configuration, testing two different values of the inter-distance between the impact points of the laser beam and the electric arc to compare the effects on microstructure and mechanical properties. Metallurgical and mechanical characterizations, performed with the specific objective of identifying the best procedure to optimize the weld features, were completed by the analysis of the theoretical thermal fields caused by the welding sources.

Metallographic investigations and EDS measurements were performed to ascertain the metallurgical features of the FZ and HAZ, assessing whether the conditions for good weldability were achieved. Mechanical properties were verified by carrying out Vickers microhardness tests and by the instrumented indentation test FIMEC (flat-top cylinder indenter for mechanical characterization), which was used to obtain the local values of the yield strength.

2. Materials and Methods

2.1. Materials

The clad steel plates, produced by hot rolling, had a total thickness of 9 mm (6.5 mm the carbon steel substrate and 2.5 mm the austenitic cladding layer). They were prepared with square edges and no gap at the substrate level, while the cladding layers were V-grooved with inclination of 45° (Figure 4a). The plates were butt-welded in horizontal

position (PA position) with the austenitic side exposed to the traveling thermal sources. The compositions of the plate and the filler wire, as given by the supplier, are shown in Table 1.

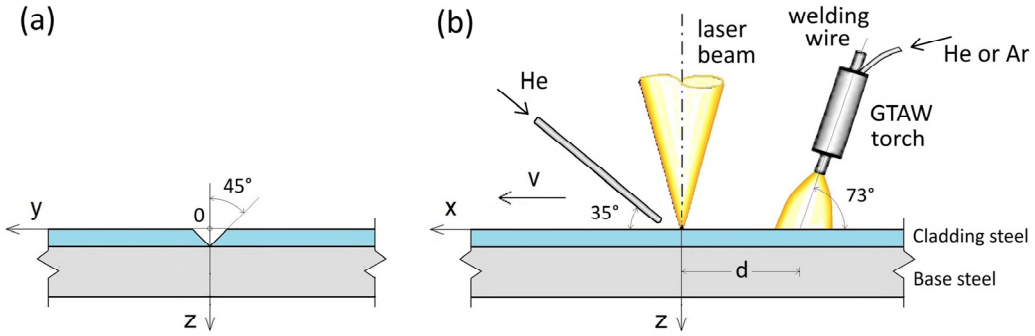


Figure 4. Welding setup: (**a**) Preparation of the two clad steel plates in the cross-section plane; (**b**) Laser-leading configuration.

Table 1. Compositions of the clad steel plates and welding wire (wt. %).

	Materials	C	Mn	Si	P	S	Cr	Ni	Mo	Cu	Fe
Plate substrate	ASTM A515 Gr.60	0.145	0.85	0.20	0.008	0.001	-	-	-	-	Bal.
Plate cladding	AISI 304L	0.017	1.32	0.39	0.029	0.003	18.39	10.07	-	-	Bal
Welding wire	DIN 1.4562 (X1NiCrMoCu 32-28-7)	0.014	1.67	0.03	-	-	27.24	29.29	6.05	1.02	Bal.

As is well documented in literature (for a review, see the article by Gupta et al. [32]), the use of Nickel-based fillers in dissimilar austenitic/ferritic joints allows us to eliminate issues such as carbon migration and the consequent metallurgical deteriorations of the interfaces. For this reason, a filler with about 30% Ni was preferred to the usual austenitic filler AWS 309L.

2.2. Process Setup

The choice of process configuration plays a fundamental role in the success of the welding and should therefore be carried out considering the specific needs. As explained in the introduction, the laser leading configuration has proven to produce a good distribution of the alloying elements coming from the electrode wire, especially in the joint zone exposed to thermal sources. For this reason, it is the most suitable to produce the required alloying action at the level of the austenitic cladding layer.

The welding trials were performed with the laser beam preceding the electric arc, both travelling at the same speed (Figure 4), using a continuous wave CO_2 laser apparatus (United Technologies, East Hartford, CT, USA) and a GMAW torch, which act simultaneously on the cladding layer side in a single pass. The torch, equipped with the welding wire, was cooled by a flux of water circulating inside the wall. The main details of the welding set-up are shown in Figure 4b.

The choice of the inter-distance between the two heat sources was made with the aim of limiting, in the portion of the joint including the cladding layer, the contribution of carbon steel in the dilution process. Therefore, as will be discussed in Section 2.3, two different values, 8 mm (Procedure A) and 55 mm (Procedure B), were adopted for a useful comparison.

2.3. Welding Parameters

The welding speed v = 1.2 m/min and the wire feeding rate equal to 15 m/min were the same for each procedure. The other welding parameters are given in Table 2.

Table 2. Welding parameters for the two procedures.

	Procedure A (d = 8 mm)	**Procedure B (d = 55 mm)**
	LBW	
Power (kW)	5	5
Focal diameter (mm)	0.5	0.5
Defocusing (mm)	0	0
Distance beam/arc (mm)	8	55
Shielding gas (L/min)	([1])	30 (He)
Welding speed (m/s)	0.02	0.02
	GMAW	
Voltage (V)	38.2	38.3
Current (A)	307	472
Power (kW)	11.7	18.1
Wire diameter (mm)	1.2	1.2
Wire feeding rate (m/s)	0.25	0.25
Shielding gas (L/min)	60 (He)	15 (Ar)
	Cumulative parameters	
LBW/GMAW power ratio	5/11.7 = 0.43	5/18.1 = 0.28
LBW + GMAW power (kW)	16.7	23.1
Welding speed (m/s)	0.02	0.02
Total heat input (kJ/m)	835	1150

[1] In this case the shielding gas comes only from the torch.

The basic parameters for the laser source were chosen based on the available equipment and the experience gained in previous works [29,33].

In the literature, given the multiplicity of welding parameters, it is possible to find a variety of combinations of their values: for example, focusing on the total heat input, the values we adopted for procedure A and B, 835 and 1150 kJ/m respectively, are comparable to 935 kJ/m utilized in [13] for LAHW in single pass 10 mm thick steel plates, or to 1820 kJ/m considered in [34] for LAHW in two passes 40 mm thick steel plates.

A laser beam is utilized for welding the substrate, starting from the bottom of the groove on the cladding layer: its working parameters (0.5 mm focal point diameter, 5 kW power, and 0.02 m/s welding speed) allow this task to be accomplished in agreement with the indications given in [35].

Concerning the electric arc, the high heat input permits us to achieve high weld widths, as shown in [36]. Assuming an almost independent action of the two heat sources, a higher power of the electric arc was used in procedure B to ensure welding in the cladding layer. Furthermore, the high values of current adopted for the two procedures limit the possibility of pore formation [17]. The values set for arc voltage, wire diameter, and feeding rate, 38 V, 1.2 mm, and 0.25 m/s (15 m/min), respectively, allow us to weld in a stable way within the region of the spray arc mode [37].

The choice of d = 8 mm, adopted for procedure A, is based on the work of Kang et al. [20], who LAHWed, in a single pass, two clad stainless steel plates with different values of the inter-distance within the range 3–9 mm. They observed that as d increases, the two heat sources become sufficiently spaced so that the laser beam does not participate in the alloying action. The latter is left to the heat input of the electric arc, which acts mainly on the austenitic layer side. Consequently, the dilution with the carbon steel substrate

is reduced and the alloying element content of the upper part of the weld increases. In particular, when d > 7.5, the Cr content approaches that of the austenitic layer.

For procedure B, the choice of d = 55 mm was made considering the indication in the article by Gao et al. [23], in which the tandem mode is developed, maintaining an inter-distance of 40 mm. Indeed, a higher value of d and a lower LBW/GMAW power ratio must be chosen to obtain a tandem configuration with prevalence of the effects of the electric arc [38]. In this case the thermal field of the laser beam does not significantly influence the action of the electric arc, and the two heat sources do not overlap their effects. This condition was adopted to substantially separate the deep keyhole mode from the shallower action of the electric arc, with the aim of concentrating, as much as possible, the addition of alloying elements in the austenitic cladding layer.

2.4. Experimental Methods

To identify the optimal procedure, the weldments were first investigated by visual inspections, then the weld beads were cut to obtain cross-section specimens for the experimental trials. They consisted of macro- and micrographic optical observations (Nikon SMZ, Nikon Instruments, Tokyo, Japan) and scanning electron microscopy with energy dispersive spectroscopy (SEM-EDS) using a field emission scanning electron microscope (Quanta 450 FEG apparatus, FEI Technologies Inc., Hillsboro, OR, USA). Concerning the Vickers microhardness test (Future-Tech Corp, Vickers microhardness tester, Kawasaki, Kanagawa, Japan), ten measures were conducted for each zone. The FIMEC test, repeated three times for each zone, was carried out with a punch diameter equal to 1 mm and a constant penetration rate 0.l mm/min, using a self-built apparatus present in the laboratories of the University of Rome–Tor Vergata (see [39] for a detailed description). The micrographic observations were performed after suitable preparation by mechanical grinding and etching with Glyceregia reagent (16% HNO3, 42% HCl, 42% glycerol) by immersion for 15 s at room temperature.

2.5. Theoretical Modeling of Thermal Fields

To analyze the interaction between the thermal fields generated by the laser beam and the electric arc in the two cases (procedure A and B), the theoretical approach based on the phenomenological laws of the heat conduction was used, utilizing the analytical solutions of the thermal field for moving heat sources proposed by Rosenthal [40]. This approach, originally applied to arc welding, was subsequently extended for simulating the temperature distribution due to laser beam welding [41].

Assuming a reference system (x,y,z) with the origin fixed to the thermal source (the axes of the reference system are shown in Figure 4a,b), moving along the welding axis x on the plate surface with speed v (m/s), the 3D thermal field $T(x,y,z)$ due to a point source is given by the following equation:

$$T(x,y,z) = T_0 + \frac{Q_P}{c\,\pi\,k\,r_P} e^{-\frac{v}{2\alpha}(r_P+x)} \quad (1)$$

where T_0 is the initial temperature, Q_P is the point source power (W), c is a numeric coefficient (c = 2 for a point positioned on the surface, and c = 4 when it is inside the plate, as specified by Rosenthal [40]), k (W/mK) is the thermal conductivity, and α (m^2/s) is the diffusivity. The radial distance from the source r_P (m) is expressed by:

$$r_P = \sqrt{x^2 + y^2 + (z - z_P)^2} \quad (2)$$

with z_P being the depth of the heat source location from the upper surface of the plate.

The thermal field due to deep penetration welding is generally modelled by a mobile source uniformly distributed on a line along the plate thickness (z axis). In this case, Rosenthal's solution takes the following form:

$$T(x,y) = T_0 + \frac{Q_L}{2\,\pi\,k} e^{-\frac{v}{2\alpha}\,x}\,K_0\left(\frac{v\,r_L}{2\alpha}\right) \tag{3}$$

It expresses the 2D temperature field $T(x,y)$ on a horizontal plane xy, with Q_L (W/m) being the power per unit of the line source length, K_0 being the modified Bessel function of the second kind of order zero, and r_L (m) being the radial distance from the source in the plane xy:

$$r_L = \sqrt{x^2 + y^2} \tag{4}$$

The previous equations allow us to express the thermal field at each point of the xyz space when the reference system is fixed on the heat source. To calculate the temperature variations in a fixed point on the plate, as the mobile sources move, the following coordinate transformation along the x axis must be applied:

$$x \rightarrow \xi = x - vt \tag{5}$$

where ξ is the new coordinate along the welding axis x, v is the speed of the thermal source moving along the welding axis (welding speed), and t is the time that varies during the relative movement of the heat sources with respect to the calculation point.

The use of conductivity-based models constitutes a substantially simplified approach to the calculation of the thermal field due to welding processes, as they neglect the complex multi-physical phenomena that occur in the interaction between the mobile heat sources and the material. Therefore, according to this approach, the thermal effects of fusion welding processes can be modelled analytically if the most appropriate mobile heat sources are used. To this end, a wide variety of mobile source models based on Rosenthal's solutions have been investigated in recent decades for simulating the thermal field generated both in the case of arc welding [42] and deep penetration laser welding [43].

To compensate for the simplification inherent in this type of modeling, the use of parameterized combinations of virtual point-line sources and the setting of their key properties (layout and relative positions, distribution of power) has been proposed, so that their effects on simulated melt pool and weld cross-sections can be consistent with experimental findings [33]. This approach has already undergone basic experimental validation in the case of the full penetration keyhole mode laser beam welding with satisfactory results. An extensive comparison between the results obtained by a multi-physics numerical simulation and the theoretical one has been also performed to further strengthen the model validity [44].

For the purposes of the presented work, this thermal field modeling approach was extended to the simulation of the effects due to the combined arc-laser welding system on clad steel by reproducing the shape of the cross-section of the welds due to the superposition of the thermal effects of the laser beam followed by the electric arc, as will be described in Section 3.5.

3. Results

3.1. Visual Inspection and Macrographic Observations

Upon visual inspection, the austenitic cladding layer is clearly identifiable; the weldments obtained with the two procedures have a regular shape, without macroscopic cracks and defects, such as distortion, serious misalignments, or undercuts. The cross-sections

representing procedures A and B, respectively, identified with the same letters, are shown by the macrographs in Figure 5.

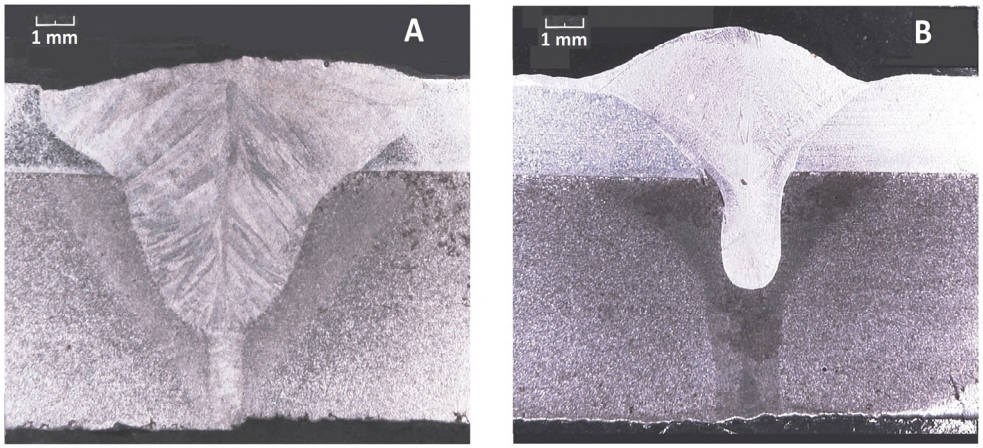


Figure 5. Cross-sections of the welds obtained with the two welding procedures (A,B).

The coupled effects of the two heat sources lead to a typical Y shaped cross-section [45], with a wider upper portion on the austenite side exposed to the arc, and a lower narrow portion on the carbon steel side exposed to the laser beam. The electric arc works in the upper portion of the weld, which is alloyed by the filler wire; while the action of the laser beam prevails as the root of the weld is approached.

The wider weld cross-section of specimen A can be intuitively ascribed to an overlapping effect of the laser beam thermal field on that of the electric arc. In procedure B, due to the high inter-distance, the thermal fields of the two heat sources are substantially separated: therefore, the weld area produced by the electric arc is reduced (here the alloying action of the filler is more effective), while the portion close to the weld root is autogenously welded by the laser beam alone.

Both procedures give a complete penetration along the entire thickness, and the welds comply with all the requirements and recommendations on quality levels in laser beam-welded steel joints according to ISO 13919-1:2019 [46]: internal imperfections (lack of fusion, cavities, incomplete penetration), surface imperfections (undercuts, weld metal excesses, toe overlap), and imperfections in joint geometry (linear misalignment) are minimal or absent. In particular, regarding the limit for undercuts and joint misalignments, the weld beads can be classified as class B.

3.2. Optical Microscopy Observations and Vickers Test

The interface between the AISI 304 L cladding layer and the ASTM A 515 base steel is highlighted by a thin line that follows the ferritic grains profile (Figure 6). The contents of Cr, Ni, and Mn decrease linearly, through a narrow diffusion layer, from the stainless steel side to the carbon steel one; the Fe atoms diffuse in the opposite direction [26]. The mobile carbon atoms diffuse over a longer distance from the ferritic steel towards the austenitic layer, where they accumulate at grain boundaries, giving rise to Cr carbide precipitation and so to the formation of a hard sensitized zone. As a result, they leave a less hard decarburized zone with coarse ferritic grains on the carbon steel side, similar to what was noted by other authors [47]. Consequently, the Vickers microhardness trend across the interface is characterized by a maximum near the cladding line on the austenitic side and a minimum on the carbon steel one (Table 3).

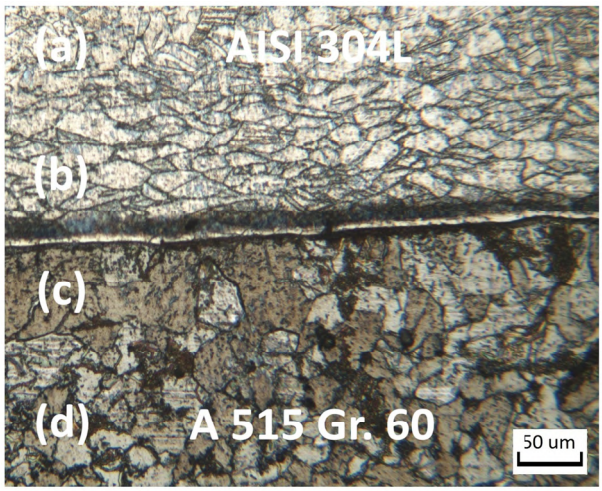


Figure 6. Optical micrograph of the interface between AISI 304 L and ASTM A515 Gr. 60 with indication of the microhardness values: (**a**) Austenitic cladding layer; (**b**) Sensitized zone; (**c**) Decarburized zone; (**d**) Base carbon steel.

Table 3. Vickers microhardness values in the cladding layer and base steel, with indications on detection zones referred to Figure 6.

Microhardness (HV)	AISI 304 L (Far from the Cladding Line)	AISI 304L (Sensitized Zone)	A 515 Gr. 60 (Far from the Cladding Line)	A 515 Gr. 60 (Decarburized Zone)
Range	179–204	248–264	131–145	122–138
Average value	198	254	143	132

In agreement with several authors [45,48] who investigated the effect of LAHW on clad steel plates, the columnar dendrites observed in Figure 5 grow from the edge of the melt pool towards the center, where the temperature is higher and the temperature gradient is smaller. As a matter of fact, the heat dissipation rate is different depending on the direction, being prevalent along the one perpendicular to the weld interface. For this reason, the grains grow faster from the fusion boundary and towards the weld centerline, assuming a columnar dendrite morphology [49].

As shown in Figure 7, the dendrites observed in specimen A consist of a fine and hard microstructure (Vickers microhardness along the centerline varies in the range 370–410 HV). Conversely, specimen B is characterized by columnar dendrites, which assume a cellular morphology in the center region (Vickers microhardness along the centerline varies in the range 150–160 HV (Table 4).

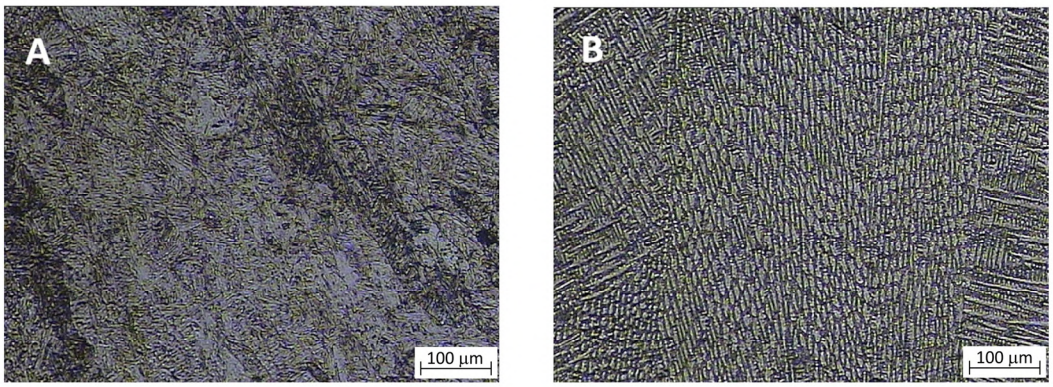


Figure 7. Dendritic microstructures of FZ near the weld centerline of the two specimens.

In both specimens, ASTM A 515 Gr. 60 steel shows a wider HAZ than AISI 304 L. As observed by Cao et al. [50], the austenitic steel has only a limited HAZ, characterized by a very thin layer with small grains, close to the fusion line, followed by slightly enlarged grains, indicating that softening occurred due to the heat input (Figure 8).

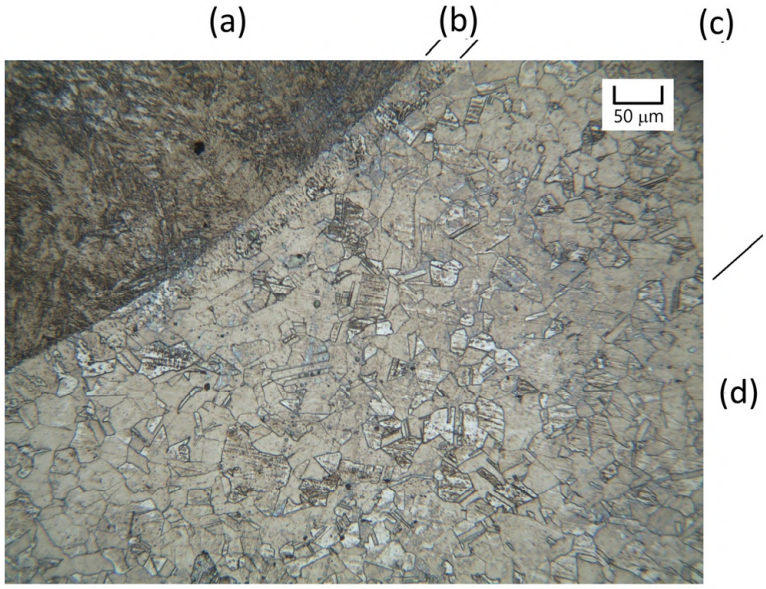


Figure 8. Optical micrograph of the interface weld/austenitic parent metal (specimen A): (**a**) Dendrites (FZ); (**b**) Thin layer with small austenitic grains (HAZ); (**c**) Slightly enlarged grains (HAZ); (**d**) Austenitic parent metal.

The formation of the HAZ mainly affects carbon steel, extending over a width of more than 1 mm in both cases A and B (Figure 5). By analyzing the HAZ at the interface with FZ (Figure 9), the different properties can be highlighted. In specimen A, ferrite and pearlite gradually transformed into a phase with Vickers microhardness reaching values around 330 HV close to the fusion line; therefore, the HAZ results harder than both the austenitic cladding layer (198 HV) and base carbon steel (143 HV). Conversely, specimen B is characterized by a softer HAZ, with microhardness in the range 155–170 HV (Table 4).

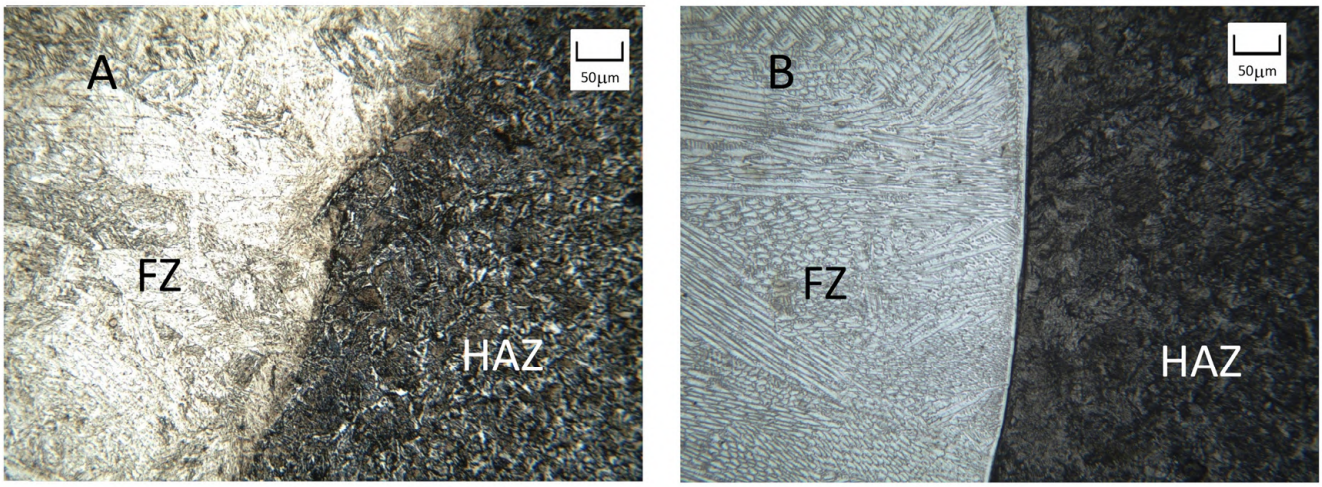


Figure 9. Optical micrographs of the interface FZ/A 515 Gr. 60 base plate for the two specimens.

Table 4. Vickers microhardness values in the FZ (alloyed zone) and HAZ (boundary with carbon steel), with indications on detection zones referred to Figures 7 and 9.

Microhardness (HV)	Specimen A FZ (Along the Weld Centerline)	Specimen A HAZ (on the Carbon Steel Side)	Specimen B FZ (Along the Weld Centerline)	Specimen B HAZ (on the Carbon Steel Side)
Range	370–410	317–345	150–160	155–170
Average value	394	330	153	164

3.3. SEM-EDS Observations

The dendritic microstructure, highlighted by visual inspections and optical microscopy observations (Figures 5 and 7), characterizes the two specimens. In particular, as shown in Figure 10, the dendrites of specimen A have a martensitic microstructure, which justifies the high values of the microhardness measured.

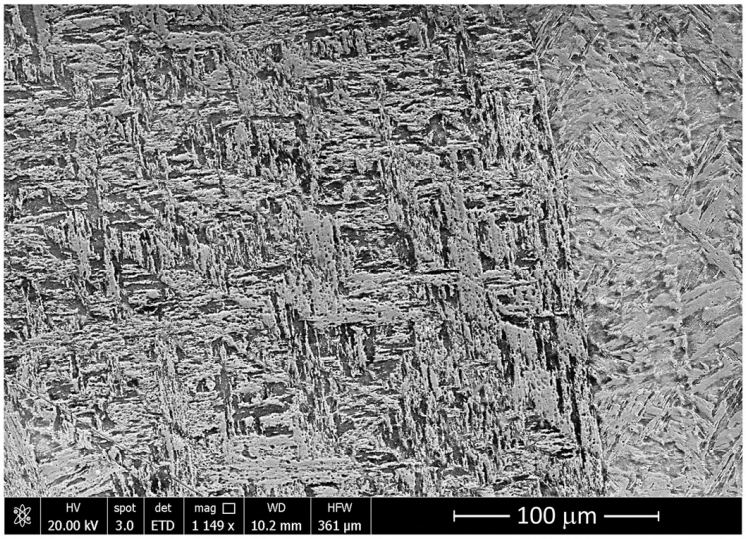


Figure 10. SEM micrograph taken on the FZ centerline of the specimen A.

The compositions resulting from SEM-EDS microanalysis in the FZ of the two specimens are given in Figure 11, together with the areas of 300 × 200 µm^2 (indicated by the orange rectangles) where these measurements were carried out.

A greater presence of alloying elements, such Ni, Cr, and Mo, can be noticed in the weld obtained with the procedure B, while carbon content is not detectable through SEM-EDS microanalysis. Furthermore, the weld composition remains substantially constant, going from the center to the lower part where the welded section narrows considerably. This high presence of alloying elements is due to the dilution between the austenitic steel and the filler, while the contribution of the carbon steel substrate is negligible. This is congruent with the findings of Kang et al. [20], previously anticipated in Section 2.3; for high values of the inter-distance, the two heat sources become sufficiently spaced so that the laser beam does not participate in the alloying effect, which can be only traced back to the electric arc, acting mainly on the austenitic layer. As a consequence, the dilution with the carbon steel substrate is reduced and the alloying elements content increases.

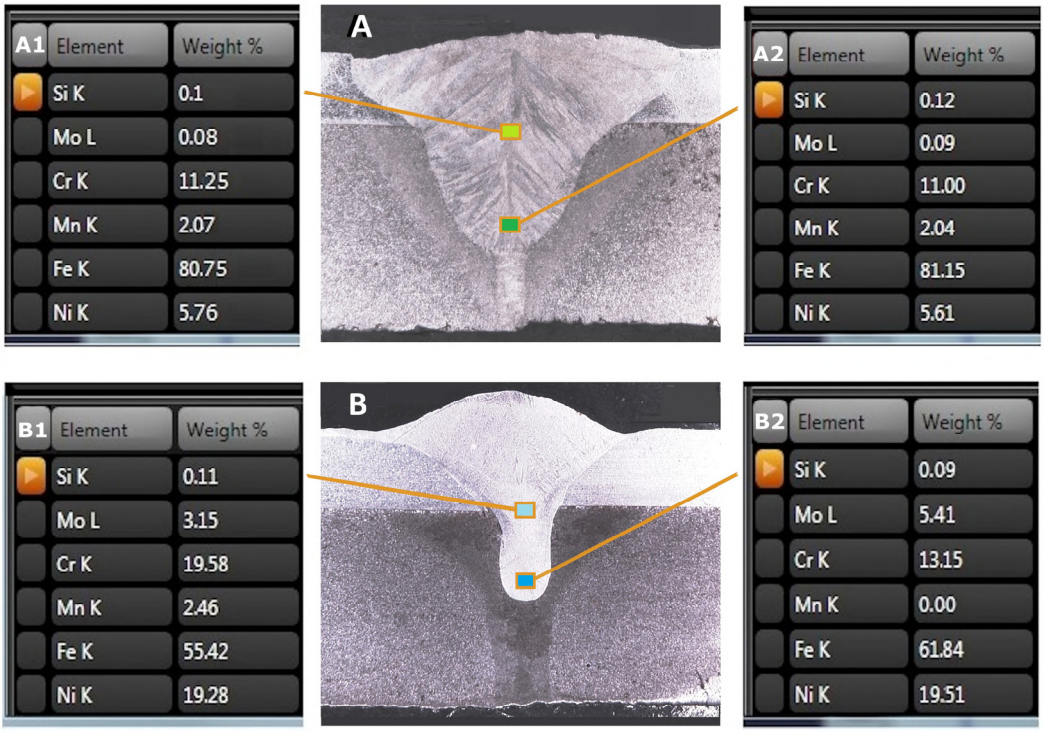


Figure 11. Results of EDS measurements on two representative points in the cross-section for both specimens (A,B).

3.4. FIMEC Test

Over the years, the FIMEC test has been taken into consideration by several authors, who experimentally verified its reliability in measuring the mechanical properties of metallic materials [39] and polymers [51], while others have turned their attention to developing models for flat indentation [52,53]. Figure 12a shows the load-penetration depth curve obtained on a 25Cr4Mo steel specimen [39], which represents the typical result of the FIMEC test: first an elastic stage of deformation occurs up to a limit pressure P_L, followed by a nearly linear plastic stage that ends at a pressure P_Y, by a stage with decreasing slope and finally by a trend with an almost constant slope. A lot of experimental results (Figure 12b) confirmed that the yield stress σ_Y, resulting from the tensile test, is approximately equal to $P_Y/3$ when the indentation rate is not higher than 0.1 mm/min (the relative difference between $P_Y/3$ and σ_Y obtained by tensile tests does not exceed ±7%).

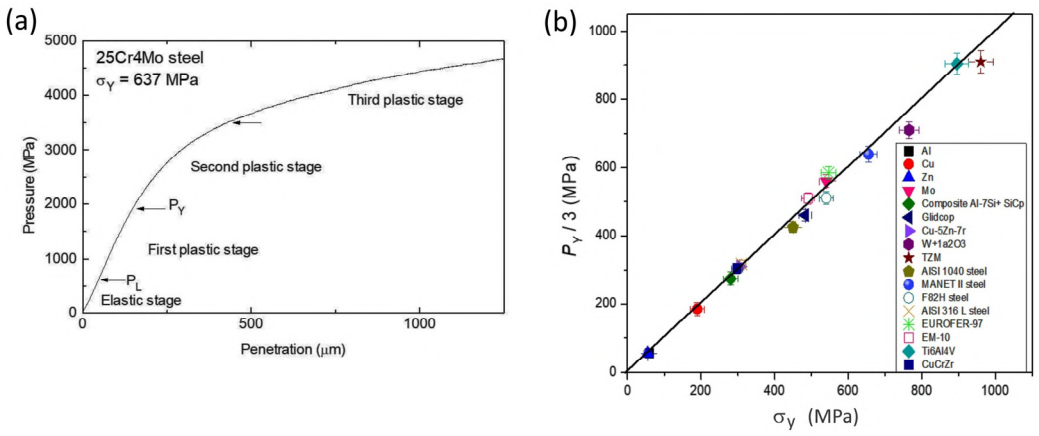


Figure 12. Results of the FIMEC test for different materials: (**a**) Typical indentation curve; (**b**) Assessment of the relationship $\sigma_Y = P_Y/3$ (Reproduced from [39]).

The results of the FIMEC test on the AISI 304 L cladding layer (CL), A515 Gr.60 base metal (BM), and on the welds (FZ) for both specimens A and B are reported in Figure 13. The load vs. penetration depth curves, carried out in different zones of the parent metals, are characterized by a good reproducibility, since they are practically superimposable; the points of the change in slope are highlighted on the curves. The $P_Y/3$ values corresponding to these curves are reported in Table 5 (with indications on the indentation points positioning). They provide an indication of the local variations in the yield strength, which reaches the highest value in the FZ of specimen A. The deviations of these values between the detected curves, on the whole, do not exceed 5%.

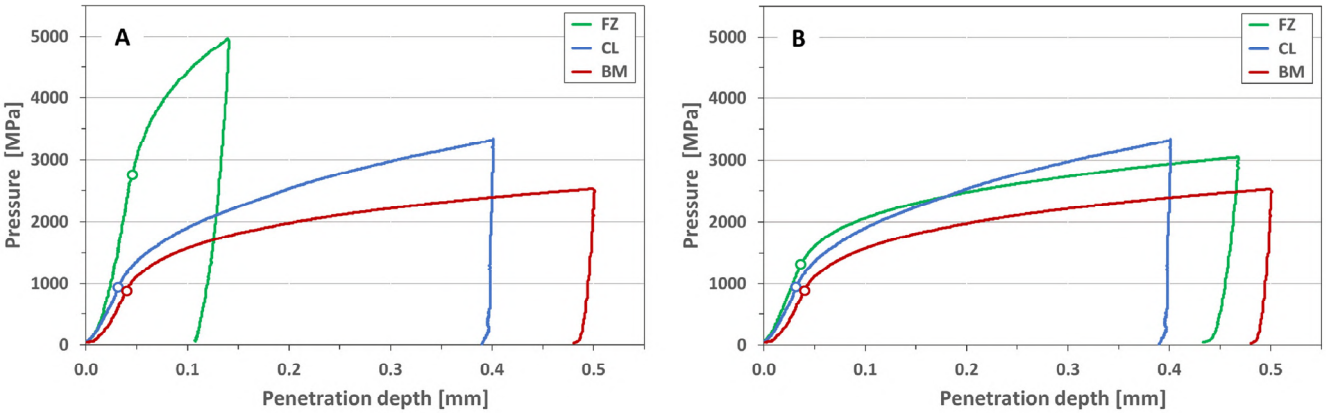


Figure 13. Results of FIMEC test for specimens (A,B).

Table 5. Values of σ_Y in MPa (calculated as $P_Y/3$).

	ASTM A515 Base Metal (Far from Weld)	AISI 304L Cladding Layer (Far from Weld)	FZ Specimen A (Weld Center)	FZ Specimen B (Weld Center)
$\sigma_Y = P_Y/3$ (MPa)	928/3 = 309	976/3 = 325	2723/3 = 907	1345/3 = 448

Finally, it is worth noting that the slope of the final trend is much more pronounced when the FIMEC test is carried out on the FZ of specimen A. This result indicates a higher brittleness, as observed in [54] for three different martensitic steels.

3.5. Thermal Field Simulation

To analyze the thermal fields generated by the heat sources in the two cases (varying the inter-distance between the leading laser and the trailing arc), their interaction, and their effect on the configurations of the weld pool and the thermal profiles to which the materials are subjected, the theoretical modelling introduced in Section 2.5 was used.

To reproduce the shape of the welds (Figure 5) due to the superposition of the thermal effects of the laser beam followed by the electric arc, the former was modelled by a line source of Equation (3) type, while the latter was modelled by a system consisting of two point sources of Equation (1) type, positioned along the z axis. For both procedures A and B, the line source, associated with high penetration keyhole mode laser welding, was considered as extended, starting from the interface between the two materials along the entire thickness of 6.5 mm of the substrate (2.5 mm < z < 9 mm), since the laser beam comes into contact with the plate at the bottom of the V-groove of the cladding layer (Figure 4a). Therefore, the power per unit length of the line source, calculated as the ratio of the power of the laser beam (5 kW from Table 2) and the length of the line source (6.5 mm), was set as Q_L = 769.23 kW/m.

The system of coupled point sources that simulate the arc welding was set differently for the two procedures:

- Procedure A—one point source on the surface at z_{P1} = 0 mm and the other one at z_{P2} = 4 mm, with the total power of the electric arc (11.7 kW from Table 2) divided between the two sources according the ratio Q_{P1}/Q_{P2} = 1.86, that is Q_{P1} = 7.61 kW and Q_{P2} = 4.09 kW;
- Procedure B—one point source on the surface at z_{P1} = 0 mm, and the other one at z_{P2} = 3 mm, with the total power of the electric arc (18.1 kW from Table 2) divided according the ratio Q_{P1}/Q_{P2} = 2.34, that is Q_{P1} = 12.68 kW and Q_{P2} = 5.42 kW.

In both cases, the values of the Q_{P1}/Q_{P2} ratio (as well as the position of the point sources, also specified in the text) were fixed to adapt the theoretical model to the real morphology of the weld bead (Figure 5), according to the assumptions on the parametric model of the virtual heat sources used, as previously discussed at the end of Section 2.5.

To achieve that, the simulated melt pool and the experimental FZ width in the cross-section at z = 2.5 mm match, arc efficiencies of 0.75 for procedure A and 0.20 for procedure B, were considered, respectively; for the laser beam, an efficiency equal to 0.55 was assumed in line with what is debated in [33]. The data on thermophysical properties of the materials used for the simulations are shown in Table 6. They were assumed as constant and referred to an intermediate temperature between room and melting temperatures, set equal to 700 °C, and were estimated based on the specific indications provided in the literature for the clad steel [55] and the base steel [56].

Table 6. Thermophysical properties of clad and base steels.

Material	Density ρ (kg/m^3)	Specific Heat C_P (J/kg°C)	Conductivity k (W/m°C)	Diffusivity $\alpha = k/\rho C_P$ (m^2/s)	Melting Temp. T_m (°C)
AISI 304 L	7682	600	25	$5.42 \cdot 10^{-6}$	1400
ASTM A515 Gr.60	7650	768	28	$4.76 \cdot 10^{-6}$	1510

Results are shown in Figure 14, where some representative xy plane isotherms, at the interface between the cladding layer and the base metal (z = 2.5 mm), are drawn: the one for T = T_m = 1455 °C (average value of the melting temperatures of the two materials at the interface) defines the contours of the melt pool sections (filled shapes in red); the other two isotherms are shown for T = 850 °C and 500 °C (range of carbide precipitation).

The maximum width of the melt pools at the cladding layer/base metal interface is approximately 6 and 2 mm for procedure A and B, respectively, in agreement with the macrographic observations (Figure 5). This confirms that the combinations of virtual point-line sources used in the theoretical model and the setting of their key parameters (layout and relative positions, distribution of power) simulate melt pools and overall weld cross-sections that are consistent with the experimental detections of weld seam shapes (in accordance with the premises on the adopted theoretical model, specified in Section 2.5).

By applying the coordinate transformation (5) in the equations of type (1) and (3), used to model the heat sources, the temperature profile of points at the interface between the cladding layer and the base metal (z = 2.5 mm), fixed on a line orthogonal to the welding line at the interface, can be calculated as a function of time, i.e., during the movement of the thermal sources along the welding axis x with the velocity v. These profiles represent the thermal cycles to which the fixed points are subjected during the movement of the sources. In Figure 15, the temperature profiles are reported for points at different distance y from the welding axis x, starting from the limit of FZ (y = 3.05 mm and y = 1.02 mm for procedure A and B, respectively), up to y = 5 mm.

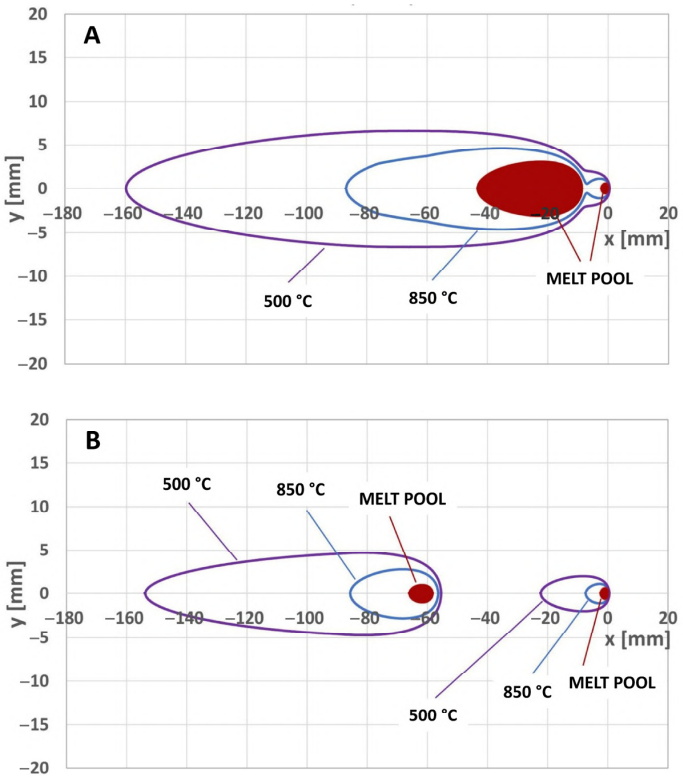


Figure 14. Thermal simulation results for the two procedures: melt pools (filled shapes with contours at T = T_m) and isotherms at 850 °C and 500 °C in the xy plane, calculated at the interface between the cladding layer and the base metal (z = 2.5 mm).

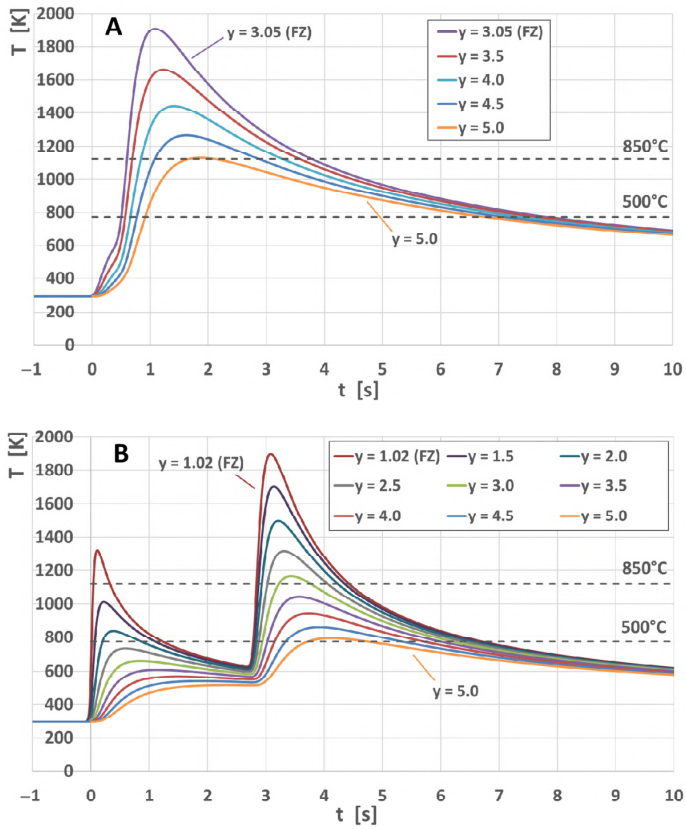


Figure 15. Thermal simulation results for the two procedures: temperature profiles for fixed points located at the interface between the cladding layer and the base metal (z = 2.5 mm), parameterized according to the y coordinate (distance of the point from the welding line at the interface).

4. Discussion

As was said in the introduction, many authors have utilized a laser-arc inter-distance below 4 mm to ensure a synergic effect between the heat sources. In this regard, Bunaziv et al. [22] performed hybrid welds on thick HSLA steel plates under different conditions, with the aim of carrying out generalizable considerations. In this way, they demonstrated that the laser-arc inter-distance is a crucial parameter: for a deep penetration, they found that the optimal values of d are different in the case of leading laser or leading arc configurations.

For the same plates in [22], the authors verified experimentally [57] that, with a leading pulsed arc, an increased inter-distance in the range from 4 to 8 mm results in higher penetration depth. With a trailing arc, shorter values of d are preferable because they allow an improved melt flow, favorable to the inward motion of the alloying elements. In this case, values of d greater than 2 mm reduce the depth of the zone affected by the alloying action of the filler metal.

Furthermore, as observed by Reutzel et al. [30] for the leading laser configuration, distances greater than 6 mm can lead to complete penetration into 6 mm thick steel plates, giving rise to two separated fusion zones.

Similar results were found by the theoretical simulation of the thermal fields (Section 3.5). In Figure 14, for procedure A (d = 8 mm), it can be observed that the melt pools generated by the leading laser beam (on the right) and the trailing electric arc (on the left) do not overlap: this can be traced back to the shape of the isotherms for $T = T_m$, which constitute the contours of the melt pools of the two thermal sources, and are closed curves that remain separate.

This condition occurs for all the isotherms of the thermal fields generated by the two sources down to that corresponding to the temperature of 890 °C. It is the threshold temperature that marks the transition from the condition with separate isotherms (one for each thermal source) to the condition in which the isotherms merge: for temperatures below this threshold, the corresponding isotherms of the two fields come into contact and become one, forming a single closed curve, as in the cases of 850 °C and 500 °C, shown in the figure.

Even for procedure B (d = 55 mm), the two melt pools do not overlap, but in this case, the simulation shows that also the other isotherms, corresponding to the two heat sources, are distinct, highlighting that the thermal fields remain substantially separate even at the lowest temperature (500 °C).

This does not mean that the thermal fields generated by the two sources do not influence each other: in both modes A and B, the thermal field generated first by the laser beam strengthens the one subsequently generated by the electric arc, expanding the weld pool and the isotherms corresponding to the second heat source. This strengthening effect can be easily appreciated by comparing the extension of the isotherms of the thermal field generated by the electric arc in the absence and presence of the leading laser beam. It turned out to be substantial in case A, in which the inter-distance d between the two sources is reduced, and is still present but more limited in case B with high inter-distance.

As an overall result, in the cases analyzed, the values of d, equal to 8 and 55 mm, led sequentially to two distinct welds: first, the leading laser beam performed an autogenous weld along the entire thickness of the substrate; subsequently, the filling action occurred under the trailing electric arc alone. In effect, two distinct parts can be clearly identified in the cross-sections of the welds, highlighted respectively by the orange and green outlines (Figure 16):

- In the cross section of specimen A, obtained by working with d = 8 mm, the electric arc gives rise to a FZ with a large extension predominantly on the cladding layer

level (orange outline); approaching the weld root, the FZ gradually reduces until the action of the electric arc runs out. Finally, the last zone before the root maintains the shape of the first weld carried out under the keyhole condition due to the laser beam (green outline);

- In specimen B, the welded section produced by electric arc has a smaller and shallower extension, since it benefits, to a limited extent, from the thermal field produced by the laser beam because of the high inter-distance d = 55 mm. In this case, the alloying process takes place with the prevalent contribution of the filler and the cladding layer, and the shape of the first weld made by the laser beam is maintained for a greater length than that observed in specimen A.

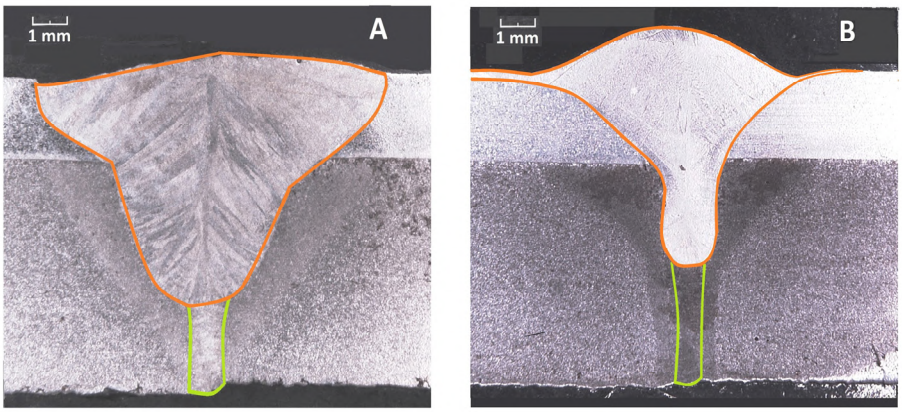


Figure 16. Cross sections of the specimens A and B, with the areas welded by the electric arc (orange) and by the laser beam (green) outlined.

The results of SEM-EDS microanalysis (Figure 11) allow us to determine the FZ microstructure through the Schaeffler diagram (Figure 17), based on the equivalent compositions expressed as percentages by weight, $Cr_{eq} = Cr + 1.5 \cdot Si + Mo + 0.5 \cdot Nb$ and $Ni_{eq} = Ni + 30 \cdot C + 0.5 \cdot Mn$, as currently carried out by researchers who investigate the welding process of dissimilar and clad steels [58,59]. The low value of carbon content in the austenitic cladding layer, base steel, and filler metal leads us to consider that its content in the FZ negligible for calculating Ni_{eq}. Therefore, using the data in Figure 11, the equivalent compositions in specimen A and B are given in Table 7.

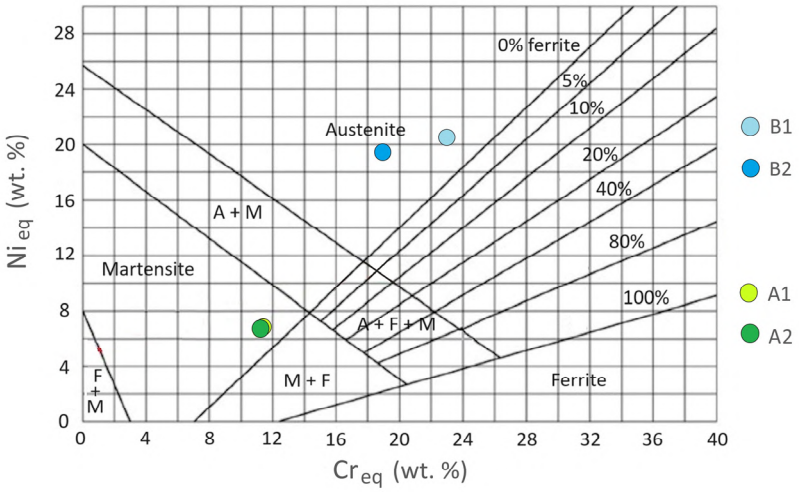


Figure 17. Schaeffler diagram with indication of the points representative of the FZ composition for the specimens A (points A1 and A2 as in Figure 11) and B (points B1 and B2 as in Figure 11).

Table 7. Equivalent compositions (wt%).

	A1	A2	B1	B2
Ni_{eq}	6.8	6.63	20.51	19.51
Cr_{eq}	11.48	11.27	22.9	18.7

As shown in Figure 17, the representative points of specimens A and B are located within the martensitic and the austenitic field, respectively (points A1 and A2 being substantially superimposable because of the corresponding values of equivalent compositions), in agreement with the metallographic observations and the results of Vickers surveys and the FIMEC test.

In conclusion, the combined welding set-up with the greater inter-distance proved to represent the most efficient configuration, as it led to a weld characterized by satisfactory mechanical properties and an austenitic microstructure, which is not affected by carbide precipitation. This last issue is clearly confirmed by the results of thermal fields simulation focused on the analysis of temperature profiles on points of the HAZ, summarized in Figure 15, which are particularly useful for evaluating the possibility of sensitization.

The temperature profiles are significantly affected by the inter-distance between the two heat sources. In procedure A, the effect is negligible, given the short time between the passage of the first source (leading laser) and the second one (trailing arc): at a speed of 0.02 m/s, the time necessary for the electric arc to reach a point previously subjected to the laser beam (i.e., to travel the 8 mm distance that separates the two sources) is equal to 0.4 s. In procedure B, the effect of the 55 mm inter-distance is clear, as the points are subject to two distinct thermal waves, spaced 2.75 s apart in time (the time necessary to travel the 55 mm inter-distance between the two sources at 0.02 m/s).

In this regard, it seems interesting to highlight that in general the use of a combined welding mode with high inter-distances, such as for procedure B, can have the advantage of compressing the exposure times to high temperatures, avoiding potentially negative effects on the HAZ, as it subjects the materials to thermal cycles broken down into distinct waves of shortened temporal amplitude.

In both the analyzed cases, it is possible to establish that, due to the short exposure times at the critical temperature range 500–850 °C for carbide precipitation (below 6 s and 4 s for procedure A and B, respectively), this phenomenon of metallurgical deterioration can be excluded [60]. This can be concluded with even greater certainty for the austenitic weld obtained with procedure B, because for carbon concentrations around 0.05%, as can occur in the molten zone due to the dilution between filler, cladding layer, and base steel, the precipitation of carbides between 850 and 500 °C requires times of several minutes or more, much longer than the few seconds calculated by the simulation.

5. Conclusions

A careful evaluation of the weldability of austenitic clad steel plates, joined by combining the action of LBW and GMAW, was carried out. The LAHW process, widely recognized in the literature as highly efficient and sustainable, was confirmed to be suitable for welding thick plates in a single pass and using a single filler material. The metallurgical and mechanical characterization performed on the welds demonstrated that a correct choice of welding setup and high Cr-Ni filler metal allows us to obtain a satisfactory joint.

In particular, the leading laser beam configuration with an inter-distance of 55 mm showed low interaction between the thermal fields generated by the two heat sources and provided better results than the configuration in which they were closely overlapped (inter-distance of 8 mm). At the larger inter-distance, the action of the leading laser beam in deep keyhole mode was substantially separate from the more superficial action of the trailing

electric arc; consequently, the contribution of the carbon steel to dilution on the cladding layer level was negligible. For this reason, the addition of alloying elements, performed by melting the filler wire, was concentrated in the austenitic cladding layer, while the laser beam acts in depth along the thickness, welding the base steel in an autogenous way.

The set-up with smaller inter-distance led to a weld characterized by a hard and brittle martensitic microstructure, while that obtained with the higher inter-distance showed satisfactory mechanical properties and an austenitic microstructure, in which carbide precipitation can be excluded due to the very short time of permanence within the sensitization range of temperature.

Author Contributions: Conceptualization, G.C., F.G., S.M., C.S., A.S. and M.E.T.; methodology, G.C., F.G., S.M., C.S., A.S. and M.E.T.; validation, G.C., F.G., S.M., C.S., A.S. and M.E.T.; formal analysis, G.C., F.G., A.S. and M.E.T.; investigation, G.C., F.G., S.M., C.S., A.S. and M.E.T.; resources, G.C., F.G., S.M., C.S., A.S. and M.E.T.; data curation, G.C., F.G., S.M., C.S., A.S. and M.E.T.; writing—original draft preparation, F.G. and A.S.; writing—review and editing, G.C., F.G., S.M., C.S., A.S. and M.E.T.; visualization, G.C., F.G., S.M., C.S., A.S. and M.E.T.; supervision, A.S. All authors have read and agreed to the published version of the manuscript.

Funding: This research was partly funded by the University of Catania, Italy, within the plan "PIAno di inCEntivi per la RIcerca di Ateneo 2024/2026", action line 1 "Progetti di ricerca collaborativa", project "INTERMETA—INterazione tra campi TERmici e leghe METAlliche nei processi per fusione: Simulazione e analisi parametrica", Department of Civil Engineering and Architecture.

Data Availability Statement: The data presented in this study are available on request from the corresponding authors.

Conflicts of Interest: The authors declare no conflicts of interest.

References

1. Bunaziv, I.; Akselsen, O.M.; Frostevarg, J.; Kaplan, A.F.H. Application of laser-arc hybrid welding of steel for low temperature service. *Int. J. Adv. Manuf. Techol.* **2019**, *102*, 2601–2613. [CrossRef]
2. Tang, G.; Zhao, X.; Li, R.; Liang, Y.; Jiang, Y.; Chen, H. The effect of arc position on laser-arc hybrid welding of 12-mm-thick high strength bainitic steel. *Opt. Laser Technol.* **2020**, *121*, 105780. [CrossRef]
3. Acherjee, B. Laser arc hybrid welding. In *Advances in Laser Materials Processing: Technology, Research and Applications*, 2nd ed.; Lawrence, J.R., Ed.; Woodhead Publishing: Cambridge, UK, 2018; pp. 203–234.
4. Bunaziv, I.; Dørum, C.; Nielsen, S.E.; Suikkanen, P.; Ren, X.; Nyhus, B.; Eriksson, M.; Akselsen, O.M. Laser-arc hybrid welding of 12- and 15-mm thick structural steel. *Int. J. Adv. Manuf. Techol.* **2020**, *107*, 2649–2669. [CrossRef]
5. Kim, S.H.; Kim, J.-D.; Jun, H.-U.; Cheon, J.-Y.; Yun, S.; Kim, Y.; Ji, C. A review on effects of weld porosity in laser-arc hybrid welding for aluminum alloys. *J. Weld. Join.* **2023**, *41*, 358–366. [CrossRef]
6. Urbanczy, M.; Adamiec, J. Hybrid welding (Laser–Electric Arc MAG) of high yield point steel S960QL. *Materials* **2021**, *14*, 5447. [CrossRef]
7. Kah, P. Overview of the exploration status of laser-arc hybrid welding processes. *Rev. Adv. Mater. Sci.* **2012**, *30*, 112–132.
8. Gook, S.; El-Batahgy, A.-M.; Gumenyuk, A.; Biegler, M.; Rethmeier, M. Application of hybrid laser arc welding for construction of LNG tanks made of thick cryogenic 9% Ni steel plates. *Lasers Manuf. Mater. Process* **2023**, *10*, 659–680. [CrossRef]
9. Zhan, X.; Wu, Y.; Kang, Y.; Liu, X.; Chen, X. Simulated and experimental studies of laser-MIG hybrid welding for plate-pipe dissimilar steel. *Int. J. Adv. Manuf. Technol.* **2019**, *101*, 1611–1622. [CrossRef]
10. Zhang, L.; Peng, G.; Chi, J.; Bi, J.; Yuan, X.; Li, W.; Zhang, L. Effect of process parameters on the formability, microstructure, and mechanical properties of laser-arc hybrid welding of Q355B steel. *Materials* **2023**, *16*, 4253. [CrossRef]
11. Brunner-Schwer, C.; Ustundag, O.; Bakir, N.; Gumenyuk, A.; Rethmeier, M. Process advantages of laser hybrid welding compared to conventional arc-based welding processes for joining thick steel structures of wind tower. *IOP Conf. Ser. Mater. Sci. Eng.* **2023**, *1296*, 012028. [CrossRef]
12. Bunaziv, I.; Ren, X.; Olden, V. A comparative study of laser-arc hybrid welding with arc welding for fabrication of offshore substructures. *J. Phys. Conf. Ser.* **2023**, *2626*, 012033. [CrossRef]
13. Abilash, M.; Senthil Kumar, D.; Padmanabham, G.; Padmanaban, P.R.; Thirumalini, S. The effect of welding direction in CO_2 LASER—MIG hybrid welding of mild steel plates. *IOP Conf. Ser. Mater. Sci. Eng.* **2016**, *149*, 012031. [CrossRef]

14. Kah, P.; Salminen, A.; Martikainen, J. The effect of the relative location of laser beam with arc in different hybrid welding processes. *Mechanicka* **2010**, *83*, 68–74.
15. Chen, Y.; Yang, Z.; Xu, K.; He, P.; Shi, M.; Chen, S.; Fang, C. Effect of energy parameters on droplet transfer behavior and weld formation in laser-arc hybrid welding with cable-type welding wire. *J. Mater. Res. Technol.* **2023**, *26*, 4191–4205. [CrossRef]
16. Ning, J.; Na, S.-J.; Wang, C.H.; Zhang, L.-J. A comparison of laser-metal inert gas hybrid welding and metal inert gas welding of high nitrogen austenitic stainless steel. *J. Mater. Res. Technol.* **2021**, *13*, 1841–1854. [CrossRef]
17. Yang, S.; Yang, L.; Wang, D.; Zhang, F.; Liu, C.; Huang, G. Effect of welding stability on process porosity in laser arc hybrid welding of dissimilar steel. *Optik* **2022**, *271*, 170165. [CrossRef]
18. Silva, R.G.N.; de Paço, C.M.M.; Rodrigues, M.B.; Sá de Sousa, J.M.; Pereira, M.; Ramos, B.B.; Barancelli Schwedersky, M.; Gonçalves e Silva, R.H. A comparison between LBW and hybrid laser-GMAW processes based on microstructure and weld geometry for hardenable steels. *Int. J. Adv. Manuf. Techol* **2020**, *110*, 2801–2814. [CrossRef]
19. Frostevarg, J.; Kaplan, A.F.H. Undercut suppression in laser-arc hybrid welding by melt pool tailoring. *J. Laser Appl.* **2014**, *26*, 031501. [CrossRef]
20. Kang, K.; Kawahito, Y.; Gao, M.; Zeng, X. Effects of laser-arc distance on corrosion behavior of single-pass hybrid welded stainless clad steel plate. *Mater. Des.* **2017**, *123*, 80–88. [CrossRef]
21. Gao, M.; Zeng, X.Y.; Hu, Q.W. Effects of welding parameters on melting energy of CO_2 laser–GMA hybrid welding. *Sci. Technol. Weld. Joi* **2006**, *11*, 517–522. [CrossRef]
22. Bunaziv, I.; Frostevarg, J.; Akselsen, O.M.; Kaplan, A.F.H. Process stability during fiber laser-arc hybrid welding of thick steel plates. *Opt. Laser Eng.* **2018**, *3*, 34–44. [CrossRef]
23. Gao, Y.; Zhang, Y.; Li, J.; Liu, K.; Xu, Y.; Zhou, J.-P. Research on the performance of laser-MIG arc tandem welding of CP-Ti/304 stainless steel bimetallic sheets. *Mater. Lett.* **2021**, *305*, 130805. [CrossRef]
24. DebRoy, T.; Elmer, J.W. Metals beyond tomorrow: Balancing supply, demand, sustainability, substitution, and innovations. *Mater. Today* **2024**, *80*, 737–757. [CrossRef]
25. Costanza, G.; Crupi, V.; Guglielmino, E.; Sili, A.; Tata, M.E. Metallurgical characterization of an explosion welded aluminum/steel joint. *Met. Ital.* **2016**, *108*, 17–22.
26. Giudice, F.; Missori, S.; Murdolo, F.; Sili, A. Metallurgical characterization of the interfaces in steel plates clad with austenitic steel or high Ni alloys by hot rolling. *Metals* **2020**, *10*, 286. [CrossRef]
27. Yu, W.X.; Liu, B.X.; Chen, C.X.; Liu, M.Y.; Zhang, X.; Fang, W.; Ji, P.G.; He, J.N.; Yin, F.X. Microstructure and mechanical properties of stainless steel clad plate welding joints by different welding processes. *Sci. Technol. Weld. Join.* **2020**, *25*, 571–580. [CrossRef]
28. Ban, H.; Yang, X.; Shi, Y.; Chung, K.-F.; Hu, Y.-F. Micro-macro properties of stainless-clad bimetallic steel welded connections with different configurations. *J. Constr. Steel Res.* **2024**, *217*, 108637. [CrossRef]
29. Missori, S.; Sili, A. Prediction of weld metal microstructure in laser beam welded clad steel. *Metallurgist* **2018**, *62*, 84–92. [CrossRef]
30. Reutzel, E.W.; Kelly, S.M.; Sullivan, M.J.; Huang, T.D.; Kvidahl, L.; Martukanitz, R.P. Hybrid laser-GMA welding for improved affordability. *J. Ship Prod.* **2008**, *24*, 72–81. [CrossRef]
31. Giudice, F.; Missori, S.; Scolaro, C.; Sili, A. A Review on metallurgical issues in the production and welding processes of clad steels. *Materials* **2024**, *17*, 4420. [CrossRef]
32. Gupta, A.; Singh, J.; Chhibber, R. Dissimilar welding of austenitic and ferritic steels using nickel and stainless-steel filler: Associated issues. *P. I Mech. Eng. E-J. Pro* **2023**, *238*, 2524–2544. [CrossRef]
33. Giudice, F.; Missori, S.; Sili, A. Parameterized multipoint-line analytical modeling of a mobile heat source for thermal field prediction in laser beam welding. *Int. J. Adv. Manuf. Technol.* **2021**, *112*, 1339–1358. [CrossRef]
34. Bunaziv, I.; Akselsen, O.M.; Frostevarg, J.; Kaplan, A.F.H. Laser-arc hybrid welding of thick HSLA steel. *J. Mater. Process Technol.* **2018**, *259*, 75–87. [CrossRef]
35. Katayama, S.; Kawahito, Y.; Mizutani, M. Elucidation of laser welding phenomena and factors affecting weld penetration and welding defects. *Phys. Procedia* **2010**, *5*, 9–17. [CrossRef]
36. Yang, S.; Wang, D.; Yang, L.; Zhang, F.; Zhang, C.; Zhou, B.; Liu, C.; Huang, G. Effects of laser-arc hybrid welding on microstructure and mechanical properties of dissimilar steel joint. *Optik* **2022**, *268*, 169795. [CrossRef]
37. Eriksson, I.; Powell, J.; Kaplan, A. Guidelines in the choice of parameters for hybrid laser arc welding with fiber lasers. *Phys. Procedia* **2013**, *41*, 119–127. [CrossRef]
38. Acherjee, B. Hybrid laser arc welding: State-of-art review. *Opt. Laser Technol.* **2018**, *99*, 60–71. [CrossRef]
39. Montanari, R.; Varone, A. Flat-top cylinder indenter for mechanical characterization: A report of industrial applications. *Materials* **2021**, *14*, 1742. [CrossRef]
40. Rosenthal, D. The theory of moving sources of heat and its application to metal treatments. *Trans. ASME* **1946**, *68*, 849–866. [CrossRef]
41. Dowden, J.M. *The Mathematics of Thermal Modelling: An Introduction to the Theory of Laser Material Processing*; Chapman & Hall/CRC: Boca Raton, FL, USA, 2001.

42. Nasiri, M.B.; Enzinger, N. Powerful analytical solution to heat flow problem in welding. *Int. J. Therm. Sci.* **2019**, *135*, 601–612. [CrossRef]
43. Franco, A.; Romoli, L.; Musacchio, A. Modelling for predicting seam geometry in laser beam welding of stainless steel. *Int. J. Therm. Sci.* **2014**, *79*, 194–205. [CrossRef]
44. Giudice, F.; Sili, A. Validation of a theoretical model for laser welding thermal field by multi-physics numerical simulation. *Metals* **2023**, *13*, 2020. [CrossRef]
45. Meng, Y.; Kang, K.; Gao, M.; Zeng, X. Relationship between corrosion resistance and microstructure characteristic of single-pass laser-arc hybrid welded stainless clad steel plate. *Met. Mater. Trans. A* **2019**, *50*, 2817–2825. [CrossRef]
46. *ISO 13919-1:2019*; Electron and Laser-Beam Welded Joints—Requirements and Recommendations on Quality Levels for Imperfections—Part 1: Steel, Nickel, Titanium and Their Alloys. ISO International Organization for Standardization: Geneva, Switzerland, 2019.
47. Li, H.; Zhang, L.; Zhang, B.; Zhang, Q. Microstructure characterization and mechanical properties of stainless steel clad plate. *Materials* **2019**, *12*, 509. [CrossRef] [PubMed]
48. Fulong, Z.; Beibei, M.; Shuangyu, L.; Bo, C.; Fengde, L.; Guochang, L.; Wei, R.; Hong, Z. Effect of a nickel-based alloy cladding layer on the strength and toughness of the high-strength steel laser-MAG hybrid welding joint. *Mater. Res. Express* **2020**, *7*, 076501. [CrossRef]
49. Li, X.; Zhang, H. Analysis of microstructure and properties of welded joint of high nitrogen steel by hybrid welding. *Mater. Res. Express* **2019**, *6*, 045602. [CrossRef]
50. Cao, J.; Wang, Y.; Liu, X.; Xu, G.; Zeng, X.; Wei, K. Single-pass high-power laser-Arc hybrid welding of thick stainless steel clad plates: Microstructure and mechanical properties. *J. Mater. Res. Technol.* **2024**, *30*, 5733–5745. [CrossRef]
51. Di Siena, M.; Genna, S.; Moretti, P.; Ponticelli, G.S.; Venettacci, S.; Russo, P. Study of the laser-material interaction for innovative hybrid structures: Thermo-mechanical characterization of polyethylene-based polymers. *Polym. Test.* **2023**, *120*, 107947. [CrossRef]
52. Brutti, C. A theoretical model for elastic-perfectly plastic flat cylindrical punch indentation. *Mech. Mater.* **2021**, *155*, 103770. [CrossRef]
53. Han, G.; Cai, L.; Xiao, H.; Huang, M. A novel flat indentation test method for obtaining stress–strain relationships of metallic materials based on energy density equivalence. *Int. J. Solids Struct.* **2023**, *269*, 112195. [CrossRef]
54. Gondi, P.; Donato, A.; Montanari, R.; Sili, A. A miniaturized test method for the mechanical characterization of structural materials for fusion reactors. *J. Nucl. Mater.* **1996**, *233–237*, 1557–1560. [CrossRef]
55. Mills, K.C. *Recommended Values of Thermophysical Properties for Selected Commercial Alloys*; Woodhead Publishing: Cambridge, UK, 2002.
56. Miettinen, J.; Louhenkilpi, S. Calculation of thermophysical properties of carbon and low alloyed steels for modelling of solidification processes. *Met. Mater. Trans. B* **1994**, *25*, 909–916. [CrossRef]
57. Bunaziv, I.; Frostevarg, J.; Akselsen, O.M.; Kaplan, A.F.H. The penetration efficiency of thick plate laser-arc hybrid welding. *Int. J. Adv. Manuf. Technol.* **2018**, *97*, 2907–2919. [CrossRef]
58. Landowski, M.; Swierczynska, A.; Rogalski, G.; Fydrych, D. Autogenous fiber laser welding of 316L austenitic and 2304 lean duplex stainless steels. *Materials* **2020**, *13*, 2930. [CrossRef]
59. Bunaziv, I.; Ren, X.; Hagen, A.B.; Hovig, E.W.; Jevremovic, I.; Dahl, S.G. Laser beam remelting of stainless steel plate for cladding and comparison with conventional CMT process. *Int. J. Adv. Manuf. Technol.* **2023**, *127*, 911–934. [CrossRef]
60. Bunaziv, I.; Olden, V.; Akselsen, O.M. Metallurgical aspects in the welding of clad pipelines—A global outlook. *Appl. Sci.* **2019**, *9*, 3118. [CrossRef]

Disclaimer/Publisher's Note: The statements, opinions and data contained in all publications are solely those of the individual author(s) and contributor(s) and not of MDPI and/or the editor(s). MDPI and/or the editor(s) disclaim responsibility for any injury to people or property resulting from any ideas, methods, instructions or products referred to in the content.